Unusual structural rearrangement and superconductivity in infinite layer cuprate superlattices

D. Samal,[1,2,#,*] Nicolas Gauquelin,[3,#,*] Yayoi Takamura,[4] Ivan Lobato,[3] Elke Arenholz,[5] Sandra Van Aert,[3] Mark Huijben,[6] Zhicheng Zhong,[7] Jo Verbeeck,[3] Gustaaf Van Tendeloo,[3] Gertjan Koster[6,*]

[1]Institute of Physics, Sachivalaya Marg, Bhubaneswar 751005, India

[2]Homi Bhabha National Institute, Anushakti Nagar, Mumbai 400085, India

[3]EMAT, University of Antwerp, Groenenborgerlaan 171, 2020 Antwerp, Belgium

[4]Department of Materials Science and Engineering, University of California-Davis, Davis, California 95616, United States

[5]Advanced Light Source, Lawrence Berkeley National Laboratory, Berkeley, California 94720, United States

[6]Faculty of Science and Technology, MESA+ Institute for Nanotechnology, University of Twente, 7500 AE Enschede, The Netherlands

[7]Key Laboratory of Magnetic Materials Devices & Zhejiang Province Key Laboratory of Magnetic Materials and Application Technology, Ningbo Institute of Materials Technology and Engineering, Chinese Academy of Sciences, Ningbo 315201, China

[#]equally contributing authors
[*]Corresponding authors
g.koster@utwente.nl, Nicolas.Gauquelin@uantwerpen.be, dsamal@iopb.res.in

Keywords: Atomic layer engineering, infinite layer cuprates, superconductivity, X-ray absorption, scanning transmission electron microscopy.

ABSTRACT: Epitaxial stabilization of thermodynamically metastable-phases and advances in atomic control of complex oxide thin film growth can be used effectively for realizing novel phenomena and as an alternative for bulk synthesis under extreme thermodynamic conditions. Here, we investigate infinite layer (IL) based cuprate superlattices, where 7–8-unit cells of $Sr_{0.6}Ca_{0.4}CuO_2$ (SCCO) are sandwiched between ultra-thin spacer layers of $SrTiO_3$ (STO), $SrRuO_3$, or $BaCuO_2$ (BCO) and only observe superconductivity in the pure [SCCO/BCO] superlattice (SL) without spacer layers. Apparently, the insertion of an additional STO spacer layer in the latter SL prevents the occurrence of superconductivity. The observed superconductivity in [SCCO/BCO] SL is discussed in terms of a structural model involving the interplay between the CuO_2-plane and the CuO-chain similar to bulk $YBa_2Cu_3O_7$ superconductor. The structural origin was found by the identification of a metastable IL-$BaCuO_2$ variant, which deviates highly from its parent bulk crystal structure and exhibits a relatively larger out-of-plane lattice parameter (around 7 Å) when sandwiched with SCCO in the form of (SCCO/BCO) SL. However, this variant is absent when STO spacer layers are introduced between SCCO and BCLO layers. X-ray absorption spectra of the Cu L-edge for BCO exhibits a slightly higher energy satellite peak as compared to the $3d^9L$ Zhang-Rice character observed in SCCO. This result indicates the existence of contrasting plane and chain-type Cu-O blocks in SCCO and BCO respectively, which is further corroborated using annular bright field scanning transmission electron microscopy imaging. This work unravels an unexpected structure of $BaCuO_2$ which helps in realizing superconductivity in (SCCO/BCO) SL and provides a wider perspective in the growth and design of cuprate based hybrid structures.

I. INTRODUCTION:

The structural paradigm of high-T_c cuprate superconductors is built on current carrying CuO_2 planes separated by charge-reservoir (CR)-blocks (blocking/balance layers) that essentially dope these CuO_2 planes [1-4]. While the CuO_2 planes described by Cu $3dx^2$-y^2 orbitals bonded to O $2p_{xy}$ orbitals in a square-planar geometry remains similar for all cuprates, the CR chemistry varies significantly from system to system. Charge carriers are generally added to the CuO_2 plane either by alteration of the CR layer through cation substitution (Sr^{2+} ions in $La_{2-x}Sr_xCuO_4$), [5] by controlling oxygen content as in the case of $YBa_2Cu_3O_{7-\delta}$ (YBCO) [6] or by electric field induced doping effect [7-10]. Particularly, in the case of YBCO, self-doping between CuO-chains and quasi 2D-CuO_2 planes is at the heart of realizing superconductivity where the CuO-chains are known to act as CR-blocks [11,12]. The infinite layer (IL) compound $ACuO_2$ (A=Ca, Sr, or Ba) appears to be the simplest structure that holds one of the key ingredients (CuO_2 planes) for realizing high-T_c superconductivity. Its crystal structure can be viewed as an oxygen deficient perovskite where each CuO_2 plane is separated by a plane of alkaline earth ions. The Cu^{2+} ions are equatorially coordinated to four oxygen ions to form a network of corner-shared CuO_4 plaquettes in a 2D-CuO_2 plane. A schematic of this structure is shown in Figure 1(a). Despite its simple crystal structure, the chemical instability of IL compounds limits their synthesis to high pressure conditions in bulk [13,14]. The IL compounds (n = ∞) are the end member of a series $A_{n+1}Cu_nO_{2n+2}$, to which most of cuprate superconductors belong, and A_2CuO_4 (214, A=La, Sr, Ba) compound is the first undoped member in this series. Mixtures of La^{3+}:Sr^{2+} or La^{3+}:Ba^{2+} as well as oxygen vacancies lead to the desired doped (superconducting) phases. In this structure, the AO layer can exist in a rocksalt configuration (T-phase) or a fluorite-like structure (T' phase), whereas the Cu ion is coordinated by an elongated oxygen octahedron of which the energetics is determined by Jahn-

Teller physics. Very recently, a superconducting Ba_2CuO_{4-y} phase (T_c around 73 K) was isolated with unusual high hole concentration (Cu^p, $p \sim 2.4$–2.6, which is twice that found in other cuprates) and having oxygen vacancies in the plane [15]. Furthermore, the CuO_6 octahedron in Ba_2CuO_{4-y} was highly compressed exhibiting a shorter Cu-O apical distance of 1.86 Å as compared to the traditional cuprates (2.4 Å for La_2CuO_4 and 1.95 Å for Sr_2CuO_3 [16]), leading to the significant admixing of $d_{3z^2-r^2}$ orbital character near E_F to the usual $d_{x^2-y^2}$ orbital. In a following discussion in literature [17], this structural model seemed appropriate and subsequently, density functional theory calculations have captured the essential physics [16, 18]. However, experimentally high pressures and strongly oxidizing conditions are required to stabilize such unique cuprates and for exploring these novel phases.

In the early nineties, it was demonstrated that metastable tetragonal infinite layer phases could be fabricated as epitaxial strained thin films under suitable growth conditions, enabled by the *pseudomorphic* stabilizing effect of the substrates, thereby avoiding the extreme bulk synthesis conditions [19-21]. Being metastable, these films typically contain many defects, but upon further optimization of growth condition, the quality and reproducibility has improved. These works have paved the way for the design of layer-by-layer IL-based cuprate heterostructures with the prime aim to search for high-T_c superconductivity in artificial hybrid structures as well as hints of any subtle structure-property relationship in these materials [22-26]. Even more success in the ability to design artificial structures has been demonstrated in layered systems using existing superconductors, such as $(LaSr)_2CuO_4$ and the Bi-cuprates as building blocks [7,27-29] in atomic layering strategies based on molecular beam epitaxy. Next to technological advances in atomic control of artificial structure design, advancement in scanning transmission electron microscopy (STEM) instrumentation and techniques such as aberration-correction of the probe-forming lens

(condenser) has made it possible to achieve sub-angstrom sized probes to study materials in an atomic-column by atomic-column fashion. High angle annular dark field (HAADF) combined with annular bright field (ABF) imaging have made it possible to study and understand the structural ordering of the cationic (due to its contrast being proportional to the atomic number of the atom) and oxygen sub-lattices in these materials respectively [30-34].

In the context of recent research on IL cuprates, the study by Samal *et al.* [35] on $SrCuO_2$ demonstrated a remarkable change in the oxygen sublattice, *i.e.* change of oxygen position from an equatorial to apical site (from planar to chain-type structure) upon lowering the film thickness below about 5 unit cells (uc). The schematic structure of this "chain-like" structure is shown on Figure 1(b). This phenomenon was attributed to an electrostatic instability associated with the polar nature of IL cuprates that consists of opposite charged atomic planes stacked along the *c*-direction [35, 36]. The experimental realization that the geometry of the CuO_4 plaquette can be controlled precisely from an in-plane to out-of-plane configuration at the atomic scale [35,37-39] in thin film structures opens the possibility to design structures with specific functionalties, e.g. current-carrying action-layer and/or charge-reservoir balance-layer, without resorting to chemical doping/substitution. Remarkably, the observations by Castro *et al.* [40,41] of high temperature superconductivity (up to 40 K) at the interface between $CaCuO_2$ and STO insulating oxides in $CaCuO_2$/STO superlattices (SLs) grown in highly oxidizing conditions has drawn the attention of the field. Their work hypothesizes that under highly oxidizing conditions, extra oxygen ions can be incorporated in the interfacial Ca plane, providing an apical oxygen site for the Cu ions and hosts holes in the CuO_2 plane. The role of the CR block in this case was attributed to a reconstructed CaO_x composition of the Ca plane at the interface. Regarding other possible effects such as relative band alignment at $CaCuO_2$ (CCO)/STO interface and the electrostatic built-in

potential induced charge transfer to interface due to polar character of CCO was also invoked to account for any doping effects that can give rise to superconductivity in CaCuO$_2$/STO SLs. However, the hard x-ray photoelectron spectroscopy study by Aruta et al. [42] revealed that direct charge transfer between CCO and STO bands is not feasible under the band alignment condition. Further it was found that the built-in electrostatic potential is suppressed even for a 3 unit cells thick CCO block by oxygen redistribution in the alkaline earth metal interface planes. Therefore both these above effects do not contribute to the realization of superconductivity through doping. But under highly oxidizing growth condition, the oxygen coordination at the interface may be increased, resulting in hole doping of cuprate block and thus the appearance of superconductivity. Similar effects of super-oxygenation have shown increased Tc in YBCO-based films [43, 44]. Furthermore, the recent discovery of superconductivity in doped infinite-layer nickelate epitaxial thin films makes the structure even more interesting [45, 46]. These studies indicate that instead of high pressure bulk synthesis, thin film epitaxy can be effectively used to stabilize thermodynamically metastable phases for manipulating their electronic properties more precisely at the atomic scale.

In this study, we investigated the oxygen coordination of Cu and the occurrence of superconductivity for a series of artificially grown hybrid IL-BaCuO$_2$ SLs. We have fabricated superlattices (SLs) by combining single unit cell BaCuO$_2$ (BCO) layers with 8 unit cell (uc) plane-type Sr$_{0.6}$Ca$_{0.4}$CuO$_2$ (SCCO) layers in which the role of an additional ultrathin spacer layer of the band insulator SrTiO$_3$ (STO) is studied. These $[(Sr_{0.6}Ca_{0.4}CuO_2)_8/STO_{m=0,2}/(BCO)_1/STO_{m=0,2}]_{10}$ SLs were grown by pulsed laser deposition (PLD). As reference samples, containing no Ba cations, we also fabricated $[(Sr_{0.6}Ca_{0.4}CuO_2)_8/(SrRuO_3)_4]_{10}$, and $[(Sr_{0.6}Ca_{0.4}CuO_2)_8/(STO)_4]_{10}$ SLs. SrRuO$_3$ (SRO) was chosen to be 4 uc thin which is the critical limit for itinerant ferromagnetic

character in SRO thin films and below which it tends to become insulating [47,48]. Even if the CuO_2 planar structure in the SCCO layers is preserved in all SLs, we observe the occurrence of superconductivity in the case of $[(SCCO)_8/(BCO)_1]_{10}$ SL, in contrast to the insulating behavior observed for $[(SCCO)_8/(STO)_4]_{10}$ and $[(SCCO)_8/(SRO)_4]_{10}$. Further, when the close proximity between the SCCO and BCO layers is disrupted by inserting an ultrathin STO spacer-layer as in the case of $[(Sr_{0.6}Ca_{0.4}CuO_2)_8/STO_{m=2}/(BCO)_1/STO_{m=2}]_{10}$, the superconductivity disappears. In a more general context, the prime goal of this study was to design IL cuprate-based SLs that can be driven into the superconducting state by manipulating the sub-layer structural/electronic characteristics, and subsequently elucidate the possible physical mechanism. By employing electron microscopy combined with X-ray absorption spectroscopy, we identified that the BCO layers have a Cu-O chain configuration (oxygen vacancy in the CuO_2 planes), and remarkable larger out-of-plane lattice parameter (around 7 Å) when present in non-buffered [SCCO/BCO] SL. Note that earlier a similar kind of structure was noticed by Koster *et al.*[26] where the $BaCuO_2$ phase was converted to Ba_2CuO_x during pulsed laser interval thin film deposition. However, X-ray absorption spectroscopy and transport measurements were never performed on those structures to explore its origin.

II. EXPERIMENT

Thin film growth: The SLs were fabricated on (001)-oriented TiO_2-terminated STO substrates by a reflection high energy electron diffraction (RHEED) assisted PLD (KrF laser with λ=248nm) at a pulse rate of 1 Hz, and a laser fluence of 2 J/cm^2. The most homogeneous part of the laser beam was selected using a 4 by 15 mm rectangular mask and an image of the mask was created on the stoichiometric targets with a lens. Before deposition the target was pre-ablated for 2 minutes at a pulse rate of 5 Hz and laser fluence 2 J/cm^2. The substrate temperature during the growth was set

at 650^0C. *In situ* RHEED was used to monitor the growth. The observed RHEED intensity oscillations shown in Figure S1 of supplemental material (SM) [49] during growth indicate the successful control on the unit cell scale due to the layer-by-layer growth mode. To grow a complete stack of SL structures, the number of laser pulses required for each layer of a specific material was calibrated and then the growth was performed in accordance with the periodicity of the SL structure. Streaky 2D RHEED patterns were observed during the film growth (Figure S2 in SM [49]). After the deposition, the samples were cooled in a high oxygen pressure (~1 bar). Two growth recipes were applied: one set of samples were grown in an oxygen pressure of 0.3 mbar, while the second set was grown in a mixture of oxygen and ~5% ozone at a pressure of about 0.3 mbar (hereafter abbreviated as O_3-grown) to enhance the oxidation. The O_3-grown samples were subsequently annealed *ex situ* at 375^0C for 2 hours in a mixture of oxygen and ~5% ozone at a pressure of 0.3 mbar (hereinafter abbreviated as O_3-annealed).

Structural characterization: The structural characterization on the SLs was carried out by X-ray diffraction (XRD) and scanning transmission electron microscopy (STEM). STEM was performed on the X-Ant-Em instrument at the University of Antwerp. 2 independent cross-sectional samples were prepared along the [100] and [010] directions of the STO substrate to investigate in-plane anisotropy using a FEI Helios 650 Dual-beam Focused Ion Beam device and exposure to oxygen was avoided using a Kammrath and Weiss transfer box and a Gatan vacuum transfer holder as proved successful on atmosphere sensitive materials [50-53]. All the SLs under STEM investigation were O_3 annealed. A ~25 nm gold layer was sputtered on top of samples prior to the preparation of the TEM cross-section specimen in order to prevent a change of the oxygen stoichiometry during the preparation process. Satisfactory samples were prepared using very low energy ion beam thinning subsequent to a protection of the sample surface by sputtering of a 10

nm thick carbon protection layer, followed be e-beam deposition of platinum as a first step to the FIB lamella preparation procedure. The FEI Titan G3 electron microscope was equipped with an aberration corrector for the probe-forming lens as well as a high-brightness gun operated at 200 kV acceleration voltage with a beam current of around 20pA for all experiments to minimize beam damage. The STEM convergence semi-angle used was 21 mrad, providing a probe size of ~0.8 Å. The collection semi-angle ranges from 11-29 mrad and 29-160 mrad for annular bright field (ABF) and annular dark field (ADF) imaging respectively. No further data-processing was applied and the raw data is presented. The line scans presented in Figure 2 were obtained by using the following procedure: first all atomic column positions in the STEM-ABF image were identified and later refined by performing a Gaussian fitting [54]. Next, all atomic column positions of each atomic layer were identified and grouped by similar planes according to A (in red) or B (in blue) sites (Figure S5(b) in SM [49]) of the perovskite structure and used to obtain an integrated line scan through the image by using a windows of three pixels (75 picometers i.e. similar size to the electron probe) for each line. Finally, the integrated line scans were averaged over each type of atomic layer. Using this averaging, the intensity profile obtained can be used to reveal non-stoichiometry on the oxygen-containing planes and making the contrast more trustworthy and more interpretable as it is proportional to Z^{γ}, in which γ is a real number between 1.0 and 2.0 depending on the microscope settings [55].

Electrical transport measurements: Transport measurements was performed using four-probe van der Pauw method with ultrasonic bonding of aluminum wire as electrodes, in a Quantum Design physical property measurement system (PPMS).

X-ray absorption measurements: X-ray absorption (XA) spectra at RT were acquired at beamline 4.0.2 at the Advanced Light Source in total electron yield (TEY) mode by monitoring the sample

drain current. To avoid charging effects during the measurement, SLs were grown on Nb-doped (0.05% at.) STO substrates. In our experiment, the linearly polarized X-rays were incident upon the sample in a grazing incidence geometry, and the E vector was applied either in-plane ($E\perp$c-axis) or canted out of plane by 30° angle relative to the [001] direction ($\sim$E$\parallel$c-axis) of the sample, as schematically represented on Figure 6(a).

III. RESULTS AND DISCUSSION

The designed structures $[(SCCO)_8/(STO)_4]_{10}$, $[(SCCO)_8/(SRO)_4]_{10}$, $[(SCCO)_8/(BCO)_1]_{10}$ show distinct satellite peaks as seen from X-ray diffraction (Figure S3 in SM [49]), which demonstrates the structural quality of the SLs. According to STEM measurements, the roughness of the layer thicknesses is equal to +/- 1 uc which is in agreement with state-of-the-art PLD growth [56-58] and the structure of each SL is discussed separately in the following section. A model with colored dots overlaid on Figures 1.ii (a)-(d) is detailed in the caption and for clarity, a 3D structural model for each SL derived from STEM analysis is shown in Figures 1.iii (a)-(d). For the sake of brevity, we represent $[(SCCO)_8/(STO)_4]_{10}$, $[(SCCO)_8/(SRO)_4]_{10}$, $[(SCCO)_8/(BCO)_1]_{10}$ SLs as [SCCO/STO], [SCCO/SRO] and [SCCO/BCO] respectively in the succeeding section. Figure 2 presents the profiles of intensity for the three SLs taken from a region where no defects were observed over an area of a few unit cells wide in the ABF image. As described in the methods part, the contrast from the ABF image is used for localization of the oxygen column and not for identifying the heavy atom columns Sr/(Sr,Ca)/Ba (red profiles) or Ru/Ti/Cu (blue profile). For simplicity, the Sr, Ca layers of the SCCO will be assimilated and named as Sr-layers since we cannot determine the Ca content of those layers from intensity. Pure oxygen atomic positions are marked with blue lines and used as an indication of the oxygen content. Green circles show the presence of oxygen in the first SrO_x layer of the SCCO layer. For each SL, the first $(Sr,Ca)O_x$

plane of the first SCCO layer contains oxygen on top of the TiO_2-terminated layer of the STO substrate. For all SLs, the planar structure of the SCCO is evidenced by the absence of oxygen in the blue profile for the Sr layers.

The [SCCO/STO] SL structure is represented in Figures 1.ii (a) and S4 (a) in SM [49]. The SCCO and STO layers grow nicely in an epitaxial fashion and have thicknesses in the range of 7-8 uc and 3-4 uc respectively. According to the STEM measurements presented on Figure 2(a), the interfacial SrO layer between the SCCO and STO layers are rich in oxygen since both SCCO/STO interfaces contain oxygen. The planar structure of the SCCO layers and their oxygen content is confirmed by the contrast in the ABF-STEM images (Figure 2 (a)) (no contrast linked to oxygen atomic columns in apical position in the ABF-image).

Figures 1.ii (b) and S4(b) in SM [49] represent the crystal structure of the [SCCO/SRO] SL. We can notice that the SCCO and SRO layers have thicknesses in the ranges 7-8 uc and 3-4 uc respectively, although some Ruddlesden-Popper defects (not shown) do exist perpendicular to the film. Furthermore, some waviness of the SRO layers (as seen on Figure S4(b) in SM [49]) is observed mainly in the 3rd SRO layer, which might be linked to the non-homogeneous character of the SCCO layers as the presence of chain- and plane-like structures are observed in some regions. The CuO_2 region within the SCCO layer has on average a planar character, but we can notice the presence of some contrast on the oxygen columns in-between the infinite layers i.e. in the SrO_x planes (suggesting the possible presence of higher coordination (5-6) Cu sites. Contrary to the previous case, the interfacial SrOx layer between SCCO and SRO layers seems slightly under-oxygenated as can be seen in Figure 2(b) (brown circles). This statement should be taken with caution due to the non-linear contrast dependence of ABF.

Figures 1.ii (c)-(d) and S4(c) in SM [49] represent the crystal structure of the [SCCO/BCO] SL. We can notice that the SCCO and BCO layers have thicknesses in the ranges 7-8 uc and 1-2 uc respectively. Many steps can be seen as shown in Figure S5(a) (red arrows) of SM [49] suggesting that the 2 uc thicknesses are an optical illusion due to the projection character of STEM imaging. The BCO layer is mostly 1 uc thick and the SCCO has the expected planar structure with CuO_2 planes running along the film as in the case of [SCCO/STO] SL. The structure of the ultrathin BCO layer seen here is far from the expected bulk structure, nonetheless a few conclusions can be made: the CuO_2 has chain configuration as confirmed by ABF imaging (O present only when looking along the [100] direction of BCO). Surprisingly, the out-of-plane spacing between the oxygen ions from the BaO plane in the BCO layer is rather large (around 7 Å) and the Ba atoms are displaced 0.5 Å farther than the oxygen on each side of the central CuO chain (Figure 3). This result is similar to the buckling of the BaO plane observed in YBCO [59,60]. In fact, according to structural refinement of YBCO by X-ray crystallography, the Ba atom is vertically displaced by 0.32 Å (0.499 Å) relative to the apical O for fully-oxygenated (under-oxygenated) YBCO [61,62]. The origin of this incredibly large out of plane lattice spacing observed in the BCO layer will be the subject of our future work. The interface with the substrate is SrO_{1-x} for all samples, as some oxygen ions are present within the Sr plane of the first unit cell of the first SCCO layer inducing a slight over-stoichiometry as shown by green circles in Figure 2(c). However, we can notice a slight depletion in oxygen of the first TiO_{2-x} plane of the substrate for the [SCCO/BCO] SL (dashed black circle). Statements about stoichiometry should be taken as an indication due to the projection character of the technique and the sample preparation step during which the stoichiometry of the sample can be altered [11,56]. Lastly, on the buffered [SCCO/BCO] SL where a spacer STO layer is inserted in-between SCCO and BCO layers, we can observe the out-of-plane lattice parameter

for BCO layer to be 4.04 Å (Figure 3(c)) in contrast to the non-buffered [SCCO/BCO] SL in which it is found to be 7.10 Å (Figure 3(d)). Electron energy loss spectroscopy (EELS) was used for chemical characterization and to show the good epitaxial quality of the complex SL stacking consisting of [SCCO (8uc)/STO(2uc)/BCO(1uc)/STO(2uc)]nominal composition (each interface at a roughness of ± 1 uc) as shown in Figure S6 of SM [49] and this SL hereinafter is abbreviated as [SCCO/STO/BCO/STO]. To avoid strong beam damage, the data was acquired with a 69 mrad collection angle, a 19 mrad convergence angle and an acceleration voltage of 80 kV with a beam current of < 40 pA and an acquisition time of 100 ms/pixel. We suggest that due to the proximity of the SrO planes of the STO layer, the BCO layer stoichiometry might be closer to $BaCuO_{3-x}$ inducing a shrinkage of the lattice parameter in the growth direction, but this is in the process of being verified using *ab-initio* calculations. Even in this complex architecture, the SCCO layer still presents the same planar structure as in all other cases presented above.

In Figure 4, we show the electrical transport properties of the designed SLs grown. The [SCCO)/STO] SLs show relatively higher sheet resistance (R_S) as compared to the [SCCO/SRO] SL. In addition, with O_3-growth, R_S drops significantly for both kinds of SLs as compared to those grown under O_2 process gas, which could be related to a relative increase of the oxygen content due to O_3 activation. With O_3-annealing, R_S drops further, but no signature of any superconducting transition is observed down to 2 K. This is unlike the case reported by Castro *et al.*[40] where superconductivity was observed in $CaCuO_2$/STO SLs synthesized under high pressure and strong oxidizing conditions. Interestingly, a spectacular electronic effect emerges when the STO or SRO spacer layer in the designed heterostructure is replaced by a chain-type BCO layer. Figure 4(b) shows the results from transport study on [SCCO/BCO] SLs synthesized under various conditions. The salient features observed are: (i) the [SCCO/BCO] SL grown under O_2 process gas exhibits

the onset of superconductivity around 15 K; (ii) the [SCCO/BCO] SL grown under a mixture of O_2 and O_3 process gas (earlier abbreviated as O_3-grown) shows enhanced metallic conduction compared to that grown under O_2 process gas, however the superconducting transition remains similar to that of [SCCO/BCO] SL; (iii) with O_3-annealing, the metallic behavior is further enhanced and the onset of the superconducting transition temperature increases up to ~50 K, however the superconducting transition region gets widened as can be seen from temperature dependent $R_S(T)/R_S(80 K)$ and (dR_s/dT) plots in Figure S7 of SM [49]. This result suggests spatial in-homogeneities in the charge carrier distribution [63] or to a certain crystallographic disorder across different SCCO/ BCO interfaces after O_3 annealing. Further, it is to be noted from Fig.4(b) that there is an enhancement of sheet resistance close to the onset of superconducting transition which could be related to thermodynamic fluctuations of the single-electron density of states (normal phase) at the Fermi level close to T_c that suppresses the one electron conductivity [64,65]. As expected, the application of a magnetic field suppresses the onset of superconductivity from 50 K to ~42 and 37 K with H=3 and 9 T, respectively, as shown in Figure 5(a). To understand if the close proximity of the chain-type BCO layer with the plane-type SCCO layer, as determined above by STEM imaging, is crucial to promote superconductivity in the designed hybrid structure, we investigated SLs where the BCO and SCCO layers were separated by two unit cells of STO i.e.[(SCCO(8uc)/STO(2uc)/BCO(1uc)/STO(2uc)]$_{10}$, which is abbreviated earlier as [SCCO/STO/BCO/STO]. Surprisingly, no superconductivity is observed in [SCCO/STO/BCO/STO] SL, rather it is found to be insulating [Figure 5(b)]. This observation points to the fact that BCO and SCCO layers must be in direct contact for the superconductivity to be observed. The results from Castro *et al.* [41] on $CaCuO_2/SrTiO_3$ hybrids revealed that the doping of holes as a function of the distance from the CR interface is confined within about 1-2

uc. Therefore, it seems pertinent that incorporating a spacer layer of 2 uc thick between the SCCO and BCO-building blocks could prohibit the observed superconductivity. Further, it is to be noted that if the superconductivity would have arisen from BCO chains only, then it would have possibly been seen in [SCCO/STO/BCO/STO] SL (although BCO in this case has a different out of plane lattice parameter than that in superconducting [SCCO/BCO] SL). From transport measurements it is not straightforward to infer specifically as to which layer hosts superconductivity in [SCCO/BCO] SL. However through a detailed structural and X-ray absorption spectroscopy investigation, it is realized that SCCO and BCO layers adopt distinct plane- and chain-type structural arrangement. Based on conventional wisdom of cuprate physics related to the interplay between chain and plane type blocks, we conjecture that a direct coupling between the adjacent plane-like SCCO and chain-like BCO layers in [SCCO/BCO] SL is necessary to induce superconductivity more likely in the SCCO planes than the BCO chains.

To obtain information about the orbital occupancy at Cu $3d$ and O $2p$ sites that could provide insight about the origin of the observed superconductivity, we performed soft X-ray absorption (XA) spectroscopy measurements on various (O_3-annealed) cuprate SLs. XA spectra probes the density of unoccupied states by exciting electrons from core shell to an empty valence state upon irradiation with X-rays of the appropriate resonance energy and they are sensitive to orbital occupancy, symmetry, valence state, and charge transfer/carrier doping. By changing the direction of the X-ray polarization (E-vector) of the linearly polarized X-ray relative to the sample surface, one can probe the angular dependence of the empty valence states. Ideally, the Cu^{2+}ion ($3d^9$ configuration) in a square planar geometry hosts a single hole in the $3d_{x^2-y^2}$ orbital as shown schematically in the inset of Figure 6 (b). To elucidate the hole symmetry at the Cu site in the planar SCCO layer, we examined the polarization dependence of spectra taken at the Cu $L_{2,3}$ edge

that correspond to the transitions $2p_{1/2}^6 3d^9 \rightarrow 2p_{1/2}^5 3d^{10}$ *(at about 930 eV)* and

$2p_{3/2}^6 3d^9 \rightarrow 2p_{3/2}^5 3d^{10}$ *(at about 950 eV)* respectively [35,40,66-69], for [SCCO/STO] and

[SCCO/SRO] SLs as shown in Figures 6(b) and (c). The polarization effect shows a much stronger

absorption when E is aligned in-plane as compared to when it is parallel to the growth direction of

the sample. The observed large asymmetry of ~57% and ~35% for [SCCO/STO] and [SCCO/SRO]

SLs respectively (asymmetry = $(I_\parallel - I_\perp / I_\parallel + I_\perp)$ where $I_\parallel$ and $I_\perp$ represent the absorption intensity at

the L edge measured with polarizations $E \perp c$-axis and $E \parallel c$-axis of the film plane respectively)

suggests that most of the holes are present in the $d_{x^2-y^2}$ orbital at the Cu sites in the SCCO layer.

This result implies a square-planar structure of CuO_2 layer and is in agreement with the STEM

results. Further, the less pronounced asymmetry for the [SCCO/SRO] SL as compared to the

[SCCO/STO] SL can be related to the presence of higher coordination (5-6) Cu sites as established

from the STEM study. Besides the central white line L_3 peak around 930 eV corresponding to the

$2p_{1/2}^6 3d^9 \rightarrow 2p_{1/2}^5 3d^{10}$ transition, a second significantly weaker peak is observed ~4.6 eV higher

in energy (more pronounced for $E \perp c$-axis), which is attributed to small content of monovalent Cu

ions ($3d^{10}$), similar to the studies on Cu_2O [70] and oxygen deficient $YBa_2Cu_3O_x$ [11, 68, 71] where

it is attributed the $3d^{10} \rightarrow 3d^9 4s^1$ transition.

To discern the subtle electronic structure changes between the SLs involving BCO layer and non

BCO layers, we show a magnified view of the fine structure in close vicinity to the L_3 peak [Figure

7]. In addition to the L_3 peak associated with un-doped Cu site, a slightly higher energy satellite

characteristic peak around 932.7 eV is observed for [SCCO/BCO] and [SCCO/STO/BCO/STO]

SLs, while only a broad shoulder like feature around 932.5 eV is observed for [SCCO/SRO] SL

(for [SCCO/STO] SL this shoulder like feature is not that prominent). The feature around 932.5

eV is a signature for Zhang-Rice singlet (ZRS), associated with a transition from $2p^63d^9L$ → $2p^53d^{10}L$, where L denotes an additional oxygen ligand hole [11, 25, 67, 69]. The higher energy state corresponding to the ZRS as compared to the $3d^{10}$ transition is attributed to the interaction between ligand and core hole that raises the energy required to promote the core electron to the unoccupied state [67]. The spectral intensity corresponding to ZRS sensitively depends on the specific arrangement of Cu-O network and doping level. Since the [SCCO/BCO] and [SCCO/STO/BCO/STO] SLs were made out of two distinct cuprate blocks (SCCO and BCO), it was difficult to distinguish accurately the characteristic ligand hole contribution from each sub layers assuming a few nanometer probing depth for oxides by XA measurements. Clarification of this connection was obtained by examining a [(BCO)$_1$/(STO)$_3$] SL hybrid as shown in Figure 7(c). Clearly, in addition to the main $3d^9$ related peak (nominal hole at un-doped Cu^{2+} site), we observe a stronger satellite peak at a slightly higher energy as discussed above for the [SCCO/BCO] and [SCCO/STO/BCO/STO] SLs and is analogous to the observation made in slightly under-doped YBCO compounds. We can further notice a polarization dependence of this peak similar to what is observed in YBCO [68,71-72] (more along c than b-axis) revealing the $3d_{z^2-y^2}$ (chain-like) character of the BCO layer as deduced from the STEM-images (Figures 1 and 3). The presence of a slightly higher energy satellite peak in the chain-like compound has already been evidenced by Gauquelin *et al.* [11] in STEM-EELS experiments. Thus, we can decompose the complex multi-electron states surrounding $3d^9$ related peak in [SCCO/BCO] and [SCCO/STO/BCO/STO] SLs into $3d^9+3d^9L^{-1}+3d^8L^{+1}$, where ligand hole configuration L^{+1} and L^{-1} as proposed by Magnuson *et al.* [12] represent for chains (additional electron on the oxygen) and planes (missing electron on the oxygen) respectively. It has to be noted that while the electronic state surrounding $3d^9$ related peak for BCO layer with having higher energy satellite peak and

chain-like configuration (STEM structural analysis) can be attributed to a $3d^9+3d^8L^{+1}$ configuration (equivalent to the CuO chain in YBCO), the same for SCCO layer with having broad shoulder and the plane like configuration (STEM structural analysis) can be attributed to a $3d^9+3d^9L^{-1}$ configuration corresponding to the ZRS (equivalent to the CuO$_2$ planes in YBCO). We, therefore, conclude that the self-doping at the interface between BCO and SCCO sub-layers might trigger the observed superconductivity in [SCCO/BCO] SL. Finally we would like to mention that in the context of high-T$_c$ cuprates, the hybridization between Cu $d_{x^2-y^2}$ and in-plane ligand orbitals (O $2p_{xy}$) govern the essential physics. However, we note the signature of the ZRS structure for both polarizations (E⊥c and E∥c) indicating the presence of both in-plane and out-of-plane ligand hole characteristics. Although the out-of-plane ligand holes have already been observed in some of the high-T$_c$ cuprates, their role realizing superconductivity remains an important question/outstanding problem [25,66,71], and was rather thought to be detrimental for superconductivity. Remarkably, the work by Aruta et al. [25] on (Cu$_{1-\delta}$C$_\delta$)Ba$_2$CuO$_x$/CaCuO$_2$ superconducting SLs demonstrated that there exists a relatively high density of out-of-plane holes from polarized XAS spectra. These holes originating from the out-of-plane orbitals (O $2p_z$) associated with the apical oxygen in the CR block (Cu$_{1-\delta}$C$_\delta$Ba$_2$CuO$_x$) are doped into CuO$_2$ planes of IL CaCuO$_2$ layer at the interface. However, when CaCuO$_2$ thickness in the above SL structure was increased, the superconductivity got suppressed, possibly because of lack of apical oxygen ions over several CuO$_2$ atomic planes in the CaCuO$_2$ layer. Therefore, it appears that itinerant holes with out-of-plane (O $2p_z$) ligand symmetry are relevant for realizing superconductivity in cuprtaes. Indeed, recent study on superconducting Ba$_2$CuO4$_{-\delta}$, [15] with having considerable admixture of $d_{3z^2-r^2}$ orbital character, apparently suggest that the holes with out-of-plane orbital character can also cooperate to produce superconductivity.

IV. CONCLUSIONS

Based on our experimental evidence, we identify that IL-BaCuO$_2$ crystal when sandwiched with planar IL-SCCO layers in the form of a [SCCO/BCO] SL, deviates highly from its parent bulk crystal structure. We find it to have chain type structure with relatively larger out-of-plane lattice parameter (around 7 Å). However, with the insertion of stable perovskite STO in-between SCCO and BCO layers, the out-of-plane lattice parameter for BCO layer turns out to be 4.04Å (IL bulk c$_{BCO}$ ~3.888 Å) as expected for a compressive in-plane strained (bulk a$_{STO}$ < bulk a$_{BCO}$) and tensile out-of plane strained IL-BaCuO$_2$ layer. The distinct plane- and chain-type structural arrangement of SCCO and BCO layers is evident from STEM and XA investigation. Remarkably, the [SCCO/BCO] SL is found to exhibit superconductivity, on the contrary this effect disappears when the close proximity between SCCO and BCO layers is disrupted by employing a thin STO spacer layer. Further, ([SCCO/STO] and [SCCO/SRO]) SLs do not exhibit any sign of superconductivity. All these observations seemingly point to the fact that a direct coupling between the adjacent plane-like SCCO and chain-like BCO layers is necessary to induce self-doping responsible for the observed superconductivity. This is analogues to structural model of YBCO where the current carrying CuO$_2$ planes are doped by the adjacent charge reservoir CuO chains. In the context of cuprate hybrid structures, it has been reported [41] that hole-doping is confined to about 1-2 uc from the charge reservoir interface. Thererefore, it is pertinent to assume that insertion of a insulating spacer layer of 2 uc thick between the SCCO and BCO-building blocks prohibits the occurence of superconductivity as reflected in the present study. In a nutshell, by exploiting the structural and electronic properties of cuprate blocks at sub-layer level, we demonstrate the possibility to design a synthetic heterostruture that hosts superconductivity. The stabilization of an

unexpected structure of BCO subject to the sequencing of layers in the superlattice structure is an important revelation in the growth and design of IL-cuprate based hybrid structures for future research and calls further investigation to understand the underlying thermodynamics behind such structural transformation in ultrathin limit.

Acknowledgements

References

(1) B. Keimer, S. A. Kivelson, M. R. Norman, S. Uchida, and J. Zaanen, Nature **518**, 179 (2015).

(2) D. Rybicki, M. Jurkutat, S. Reichardt, C. Kapusta, and J. Haase, Nat Commun **7**, 11413 (2016).

(3) Poole, C. P. *Handbook of superconductivity*; Academic Press: London, 2000.

(4) N. Gauquelin, H. Zhang, G. Zhu, J. Y. Wei, and G. A. Botton, AIP Advances **8**, 055022 (2018).

(5) M. A. Kastner, R. J. Birgeneau, G. Shirane, and Y. Endoh, Rev. Mod. Phys. **70**, 897 (1998).

(6) Ruixing Liang, D. A. Bonn, and W. N. Hardy, Phys. Rev. B **73**, 180505 (2006).

(7) A. T. Bollinger, G. Dubuis, J. Yoon, D. Pavuna, J. Misewich and I. Božović, Nature **472**, 458–460 (2011).

(8) D. Matthey, N. Reyren, J.-M. Triscone, and T. Schneider, Phys. Rev. Lett. **98**, 057002 (2007).

(9) D. Matthey, S. Gariglio, and J.-M. Triscone, Appl. Phys. Lett. **83**, 3758-3760 (2003).

(10) M. Salluzzo, G. Ghiringhelli, J. C. Cezar, N. B. Brookes, G. M. De Luca, F. Fracassi, and R. Vaglio, Phys. Rev. Lett. **100**, 056810 (2008).

(11) N. Gauquelin, D. G. Hawthorn, G. A. Sawatzky, R. X. Liang, D. A. Bonn, W. N. Hardy and G. A. Botton, Nat Commun **5**, 4275 (2014).

(12) M. Magnuson, T. Schmitt, V. N. Strocov, J. Schlappa, A. S. Kalabukhov and L.-C. Duda, Sci Rep **4**, 7017 (2014).

(13) M. Azuma, Z. Hiroi, M. Takano, Y. Bando and Y. Takeda, Nature **356**, 775–776 (1992).

(14) H. Zhang, Y. Y. Wang, H. Zhang, V. P. Dravid, L. D. Marks, P. D. Han, D. A. Payne, P. G. Radaelli and J. D. Jorgensen, Nature **370**, 352–354 (1994).

(15) W. M. Li, J. F. Zhao, L. P. Cao, Z. Hu, Q. Z. Huang, X. C. Wang, Y. Liu, G. Q. Zhao, J. Zhang, Q. Q. Liu, R. Z. Yu, Y. W. Long, H. Wu, H. J. Lin, C. T. Chen, Z. Li, Z. Z. Gong, Z. Guguchia, J. S. Kim, G. R. Stewart, Y. J. Uemura, S. Uchida, and C. Q. Jin, PNAS **116** (25), 12156-12160 (2019).

(16) H.-S. Jin, W. E. Pickett, and K.-W. Lee, Phys. Rev. B **104**, 054516 (2021).

(17) D. J. Scalapino, PNAS **116** (25), 12129-12130 (2019).

(18) P. Worm, M. Kitatani, J. M. Tomczak, L. Si and K. Held, Phys. Rev. B **105**, 085110 (2022).

(19) M. Kanai, T. Kawai, and S. Kawai, Appl. Phys. Lett. **58**, 771-773 (1991).

(20) C. Niu and C. M. Lieber, J. Am. Chem. Soc. **114**, 9, 3570–3571 (1992).

(21) D. P. Norton, B. C. Chakoumakos, J. D. Budai, and D. H. Lowndes, Appl. Phys. Lett. **62**, 1679-1681 (1993).

(22) D. P. Norton, B. C. Chakoumakos, J. D. Budai, D. H. Lowndes, B. C. Sales, J. R. Thompson and D. K. Christen. Science **265**, 5181, 2074–2077 (1994).

(23) G. Balestrino, S. Martellucci, P. G. Medaglia, A. Paoletti, G. Petrocelli, and A. A. Varlamov, Phys. Rev. B **58**, R8925(R) (1998).

(24) G. Balestrino, G. Pasquini, and A. Tebano, Phys. Rev. B **62**, 1421 (2000).

(25) C. Aruta, G. Ghiringhelli, C. Dallera, F. Fracassi, P. G. Medaglia, A. Tebano, N. B. Brookes, L. Braicovich, and G. Balestrino, Phys. Rev. B **78**, 205120 (2008).

(26) G. Koster, A. Brinkman, H. Hilgenkamp, A. J. H. M. Rijnders and D. H. A. Blank, J. Phys.: Condens. Matter **20** 264007 (2008).

(27) A. Gozar, G. Logvenov, L. F. Kourkoutis, A. T. Bollinger, L. A. Giannuzzi, D. A. Muller and I. Bozovic, Nature **455**, 782–785 (2008).

(28) G. Logvenov, A. Gozarand and I. Bozovic, Science **326**, 699–702 (2009).

(29) J. N. Eckstein, I. Bozovic & G. F. Virshup, MRS Bulletin **19**, 44–50 (1994).

(30) N. Gauquelin , K. H. W. van den Bos , A. Béché , F. F. Krause , I. Lobato , S. Lazar , A. Rosenauer , S. Van Aert and J. Verbeeck, Ultramicroscopy **181**, 178-190 (2017).

(31) D. Kan, R. Aso, R. Sato, M. Haruta, H. Kurata and Y. Shimakawa, Nature Mater **15**, 432–437 (2016).

(32) A. Lotnyk, D. Poppitz, J. W. Gerlach, and B. Rauschenbach, Appl. Phys. Lett. **104**, 071908 (2014)

(33) S.D. Findlay, N. Shibata, H. Sawada, E. Okunishi, Y. Kondo and Y. Ikuhara, Ultramicroscopy **110(7)**, 903–923 (2010).

(34) S.D. Findlay, Y. Kohno, L.A. Cardamone, Y. Ikuhara and N. Shibata, Ultramicroscopy**,** 136, 31–41 (2014).

(35) D. Samal, H. Tan, H. Molegraaf, B. Kuiper, W. Siemons, Sara Bals, Jo Verbeeck, G. V. Tendeloo, Y. Takamura, E. Arenholz, C. A. Jenkins, G. Rijnders, and G. Koster, Phys. Rev. Lett. **111**, 096102 (2013).

(36) Z. Zhong, G. Koster, and P. J. Kelly, Phys. Rev. B **85**, 121411(R) (2012).

(37) B. Kuiper, D. Samal, D. H. A. Blank, J. E. ten Elshof, G. Rijnders, and G. Koster, APL Materials **1**, 042113 (2013).

(38) M. Dantz, J. Pelliciari, D. Samal, V. Bisogni, Y. Huang, P. Olalde-Velasco, V. N. Strocov, G. Koster & T. Schmitt, Sci Rep **6**, 32896 (2016).

(39) D. Samal and G. Koster, Journal of Materials Research **30**, 463–476 (2015).

(40) D. Di Castro, M. Salvato, A. Tebano, D. Innocenti, C. Aruta, W. Prellier, O. I. Lebedev, I. Ottaviani, N. B. Brookes, M. Minola, M. Moretti Sala, C. Mazzoli, P. G. Medaglia, G. Ghiringhelli, L. Braicovich, M. Cirillo, and G. Balestrino, Phys. Rev. B **86**, 134524 (2012).

(41) D. Di Castro, C. Cantoni, F. Ridolfi, C. Aruta, A. Tebano, N. Yang, and G. Balestrino, Phys. Rev. Lett. **115**, 147001 (2015).

(42) C. Aruta,1, C. Schlueter, T.L. Lee, D. Di Castro, D. Innocenti, A. Tebano, J. Zegenhagen, and G. Balestrino, Phys. Rev. B **87**, 155145 (2013).

(43) H. Zhang, N. Gauquelin, C. Mcmahon, D. G. Hawthorn, G. A. Botton and J. Y. T. Wei, Nanomaterials for Security, Conference proceedings, 45-56 (2016).

(44) H. Zhang, N. Gauquelin, C. McMahon, D. G. Hawthorn, G. A. Botton, and J. Y. T. Wei, Phys. Rev. Materials **2**, 033803 (2018).

(45) D. Li, K. Lee, B. Y. Wang, M. Osada, S. Crossley, H. R. Lee, Y. Cui, Y. Hikita and H. Y. Hwang, Nature **572**, 624–627 (2019).

(46) S. Zeng, C. S. Tang, X. Yin, C. Li, M. Li, Z. Huang, J. Hu, W. Liu, G. J. Omar, H. Jani, Z. S. Lim, K. Han, D. Wan, P. Yang, S. J. Pennycook, A. T. S. Wee, and A. Ariando, Phys. Rev. Lett. **125**, 147003 (2020).

(47) Jing Xia, W. Siemons, G. Koster, M. R. Beasley, and A. Kapitulnik, Phys. Rev. B **79**, 140407(R) (2009).

(48) F. Bern, M Ziese, A. Setzer, E. Pippel, D. Hesse and I. Vrejoiu, J. Phys.: Condens. Matter **25**, 496003 (2013).

(49) See Supplemental Material at [URL will be inserted by publisher] for RHEED intensity oscillation and RHEED diffraction pattern, X-ray diffraction, structural characterization by scanning transmission electron microscopy, chemical characterization by electron energy loss spectroscopy and temperature dependent resistive transition.

 (50) N. Lebedev, M. Stehno, A. Rana, P. Reith, N. Gauquelin, J. Verbeeck, H. Hilgenkamp, A. Brinkman and J. Aarts, Sci Rep **11**, 10726 (2021).

(51) D. J. Groenendijk, C. Autieri, T. C. van Thiel, W. Brzezicki, J. R. Hortensius, D. Afanasiev, N. Gauquelin, P. Barone, K. H. W. van den Bos, S. van Aert, J. Verbeeck, A. Filippetti, S. Picozzi, M. Cuoco, and A. D. Caviglia, Phys. Rev. Research **2**, 023404 (2020).

(52) R. L. Bouwmeester, K. de Hond, N. Gauquelin, J. Verbeeck, G. Koster and A. Brinkman, Phys. Status Solidi RRL **13** (7), 1800679 (2019).

(53) B. Conings, J. Drijkoningen, N. Gauquelin, A. Babayigit, J. D'Haen, L. D'Olieslaeger, A. Ethirajan, J. Verbeeck, J. Manca, E. Mosconi, F. D. Angelis, and H.-G. Boyen, Adv. Energy Mater. **5**, 1500477 (2015).

(54) A. De Backer, K.H.W. van den Bos, W. Van den Broek, J. Sijbers and S. Van Aert, Ultramicroscopy **171**, 104-116 (2016).

(55) P. Hartel, H. Rose and C. Dinges, Ultramicroscopy **63**, 93- 114 (1996).

(56) N. Gauquelin, E. Benckiser, M. K. Kinyanjui, M. Wu, Y. Lu, G. Christiani, G. Logvenov, H.-U. Habermeier, U. Kaiser, B. Keimer, and G. A. Botton, Phys. Rev. B **90**, 195140 (2014).

(57) Y. Z. Chen, F. Trier, T. Wijnands, R. J. Green, N. Gauquelin, R. Egoavil, D. V. Christensen, G. Koster, M. Huijben, N. Bovet, S. Macke, F. He, R. Sutarto, N. H. Andersen, J. A. Sulpizio, M.

Honig, G. E. D. K. Prawiroatmodjo, T. S. Jespersen, S. Linderoth, S. Ilani, J. Verbeeck, G. Van Tendeloo, G. Rijnders, G. A. Sawatzky and N. Pryds, Nature Mater **14**, 801–806 (2015).

(58) M. Huijben, Y. Liu, H. Boschker, V. Lauter, R. Egoavil, J. Verbeeck, S. G. te Velthuis, G. Rijnders, and G. Koster, Adv. Mater. Interfaces **2**, 1400416 (2015).

(59) R. Hott, R. Kleiner, T. Wolf and G. Zwicknagl (Superconducting Materials — A Topical Overview), *Frontiers in superconducting materials*; Springer: Berlin, Heidelberg, 2004; pp 1–70.

(60) C. C. Tsuei and J. R. Kirtley, Rev. Mod. Phys. **72**, 969 (2000).

(61) S. Sato, I. Nakada, T. Kohara and Y. Oda, Acta Crystallogr., Sect. C: Cryst. Struct. Commun. **44** (1), 11–14 (1988).

(62) J. S. Swinnea and H. Steinfink, Journal of Materials Research **2**, 424–426 (1987).

(63) F. Baiutti, G. Gregori, Y. E. Suyolcu, Y. Wang, G. Cristiani, W. Sigle, P. A. van Aken, G. Logvenov, and J. Maier, Nanoscale **10**, 8712 (2018).

(64) G. Balestrino, E. Milani, and C. Aruta, Phys. Rev. B 54, 3628 (1996)

(65) D. V. Livanov, E. Milani, G. Balestrino, and C. Aruta, Phys. Rev. B 55, R8701 (1997)

(66) C. T. Chen, L. H. Tjeng, J. Kwo, H. L. Kao, P. Rudolf, F. Sette, and R. M. Fleming, Phys. Rev. Lett. **68**, 2543 (1992).

(67) D. Meyers, Swarnakamal Mukherjee, J.-G. Cheng, S. Middey, J.-S. Zhou, J. B. Goodenough, B. A. Gray, J. W. Freeland, T. Saha-Dasgupta and J. Chakhalian, Sci Rep **3**, 1834 (2013).

(68) D. G. Hawthorn, K. M. Shen, J. Geck, D. C. Peets, H. Wadati, J. Okamoto, S.-W. Huang, D. J. Huang, H.-J. Lin, J. D. Denlinger, Ruixing Liang, D. A. Bonn, W. N. Hardy, and G. A. Sawatzky, Phys. Rev. B 84, 075125 (2011).

(69) D. Samal, H. Tan, Y. Takamura, W. Siemons, J. Verbeeck, G. Van Tendeloo, E. Arenholz, C. A. Jenkins, G. Rijnders, and G. Koster, EPL (Europhys. Letters) **105**, 17003 (2014).

(70) M. Grioni, J. F. van Acker, M. T. Czyžyk, and J. C. Fuggle, Phys. Rev. B **45**, 3309 (1992).

(71) N. Nücker, E. Pellegrin, P. Schweiss, J. Fink, S. L. Molodtsov, C. T. Simmons, G. Kaindl, W. Frentrup, A. Erb, and G. Müller-Vogt, Phys. Rev. B **51**, 8529 (1995).

(72) J. Fink, N. Nücker, E. Pellegrin, H. Romberg, M. Alexander, and M. Knupfer, Journal of Electron Spectroscopy and Related Phenomena **66** (3-4), 395–452 (1994).
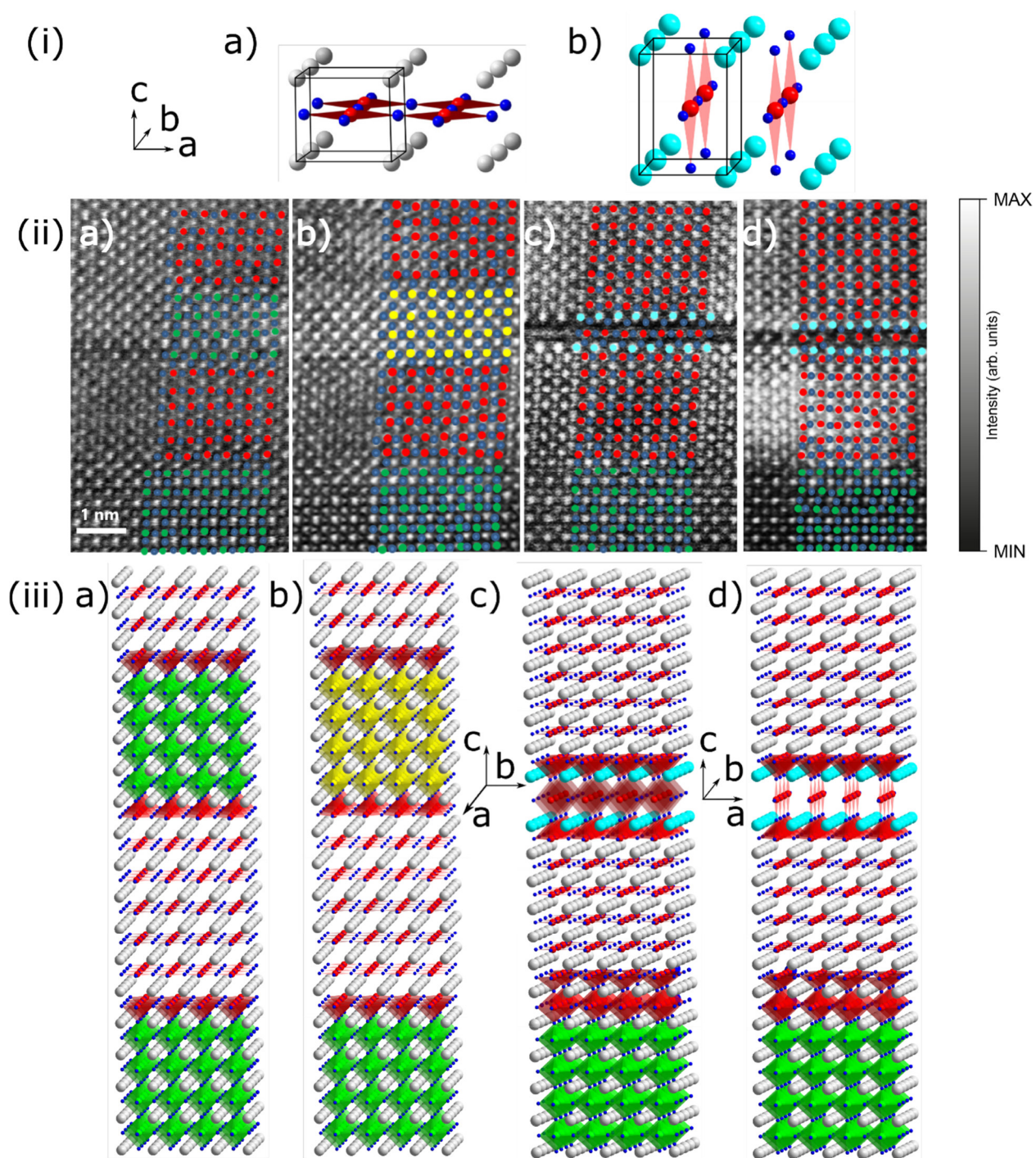
Figure 1. Structural analysis of the SLs. (i) Structural model on the same scale of **(a)** the infinite-layer compound (Sr, Ca) CuO_2 and **(b)** the expected chain-like structure of $BaCuO_2$. (ii) Raw inversed-contrast ABF-STEM image of **(a)** **[SCCO/STO]**, **(b)** **[SCCO/SRO]**, and **(c)** [SCCO/BCO] SLs imaged along [100]-zone-axis and **(d)** [SCCO/BCO] imaged along the [010] zone direction. (iii) SLs with corresponding 3D structural models as determined by STEM analysis: **(a)** [SCCO/STO], **(b)** [SCCO/SRO], **(c)** and **(d)** **[**SCCO/BCO] (two different orientations of the [SCCO/BCO] SL showing the chain structure of the BCO layer along *a* and *b* direction respectively). The MO_x polyhedra are shown in color around the central atom. The apparent skewness in the ABF images is due to scan distortions and drift of the sample during acquisition. The scanning direction is along the horizontal direction (width of the image).
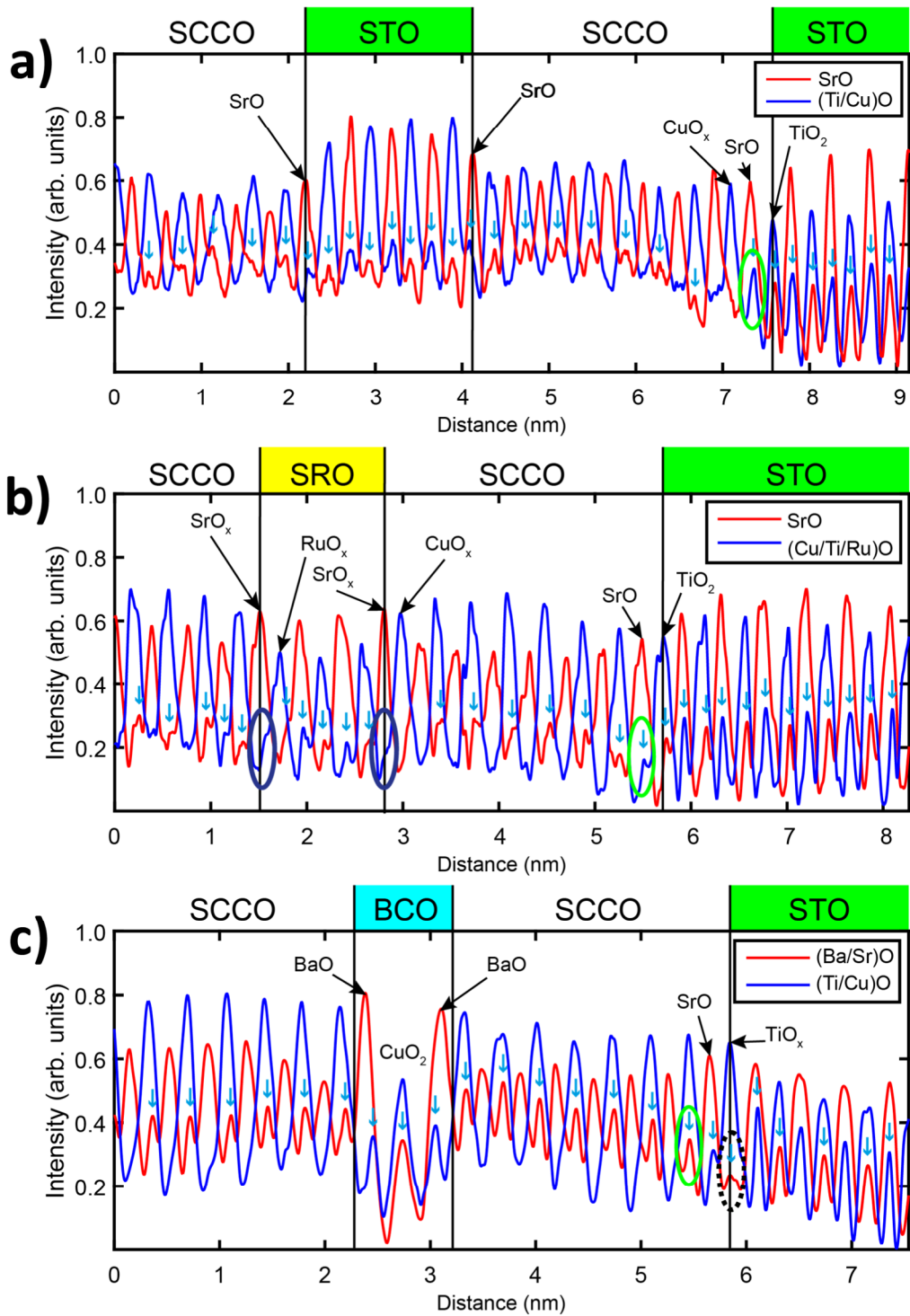
Figure 2: Comparison of line scans over the STEM-ABF images averaged across 20 of each type of atomic layers on the Sr/Ca/Ba-O (in red) and Ru/Cu/Ti-O (in blue) planes of the (a) [SCCO/STO] (b) [SCCO/SRO] and (c) [SCCO/BCO] SLs respectively showing the layering and chemistry in each layer. Oxygen atomic positions are marked with blue arrows. Green circles show the presence of oxygen in the first SrO_x layer of the SCCO, brown circles show the low oxygen content of the SrO_x planes at the interfaces between SRO and SCCO and the black dashed circle shows the oxygen depletion in the last TiO_{2-x} plane of the STO substrate for the [SCCO/BCO] SL. For each SL, the first $(Sr,Ca)O_x$ plane of the first SCCO layer contains oxygen on top of the terminal TiO_2 layer of the STO substrate. For all SLs, the planar structure of SCCO is evidenced by the abscence of oxygen in the blue profile for the Sr layers. The red (peaks) planes not directly labelled in the STO, SCCO and SRO are respectively SrO, (Sr/Ca) and SrO. The blue (peaks) planes not directly labelled in the STO, SCCO and SRO are respectively TiO_2, CuO_2 and RuO_2.
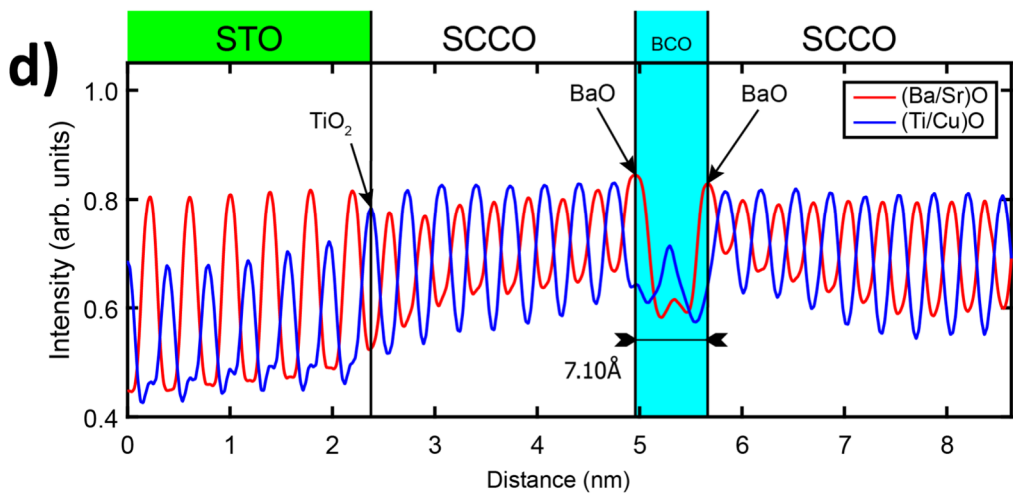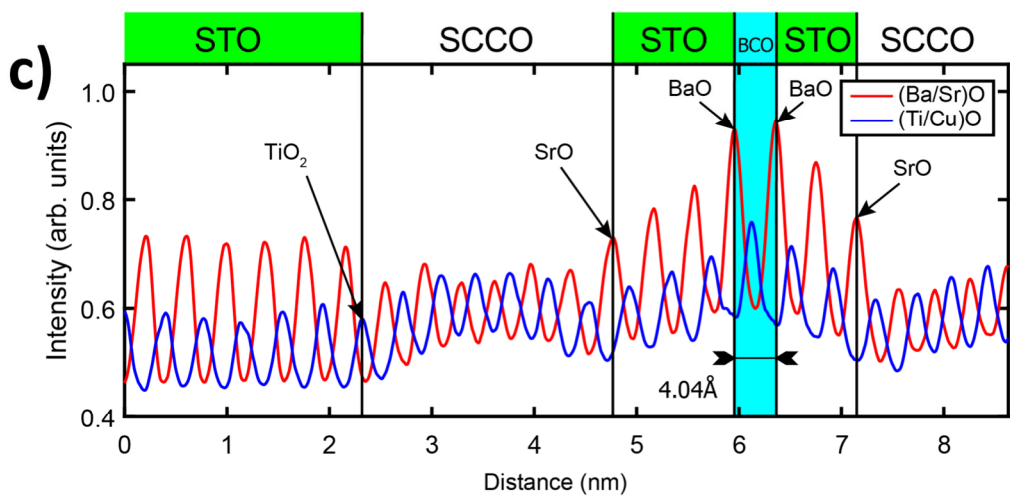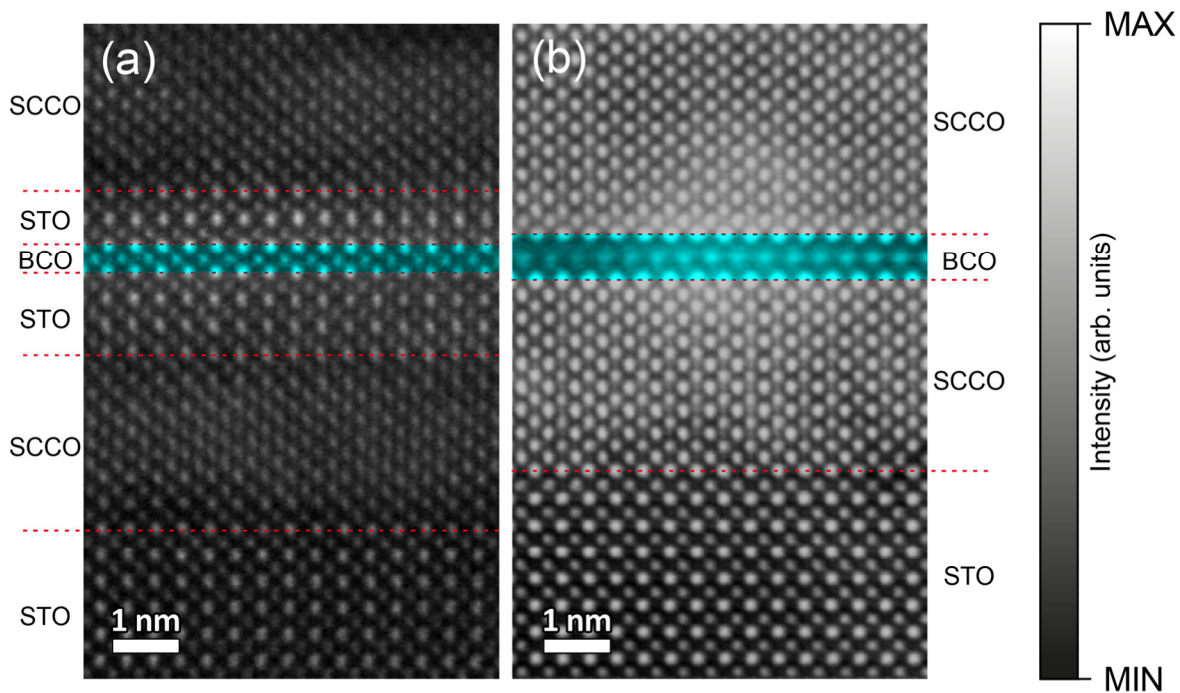
Figure 3: STEM-HAADF images resulting from averaging 20 low dose images of the (a) [SCCO/STO/BCO/STO], (b) [SCCO/BCO] SLs with the corresponding averaged line profiles ((c) and (d)) acquired as described for Fig.2. The intensity is displayed as grey scale and is proportional to the average atomic number in each columns. We can easily remark the difference in the out-of-plane lattice spacing of the BCO layer between the STO buffered insulating case (c) and the non-buffered superconducting case (d). This difference could be related to the structure difference between a perovskite environment (**Figure** 3(c)) and the chain-type structure (**Figure** 3(d)). The red (peaks) planes not directly labelled in the STO, SCCO and BCO are respectively SrO, (Sr/Ca) and BaO. The blue (peaks) planes not directly labelled in the STO, SCCO and BCO are respectively TiO_2, CuO_2 and CuO_2.
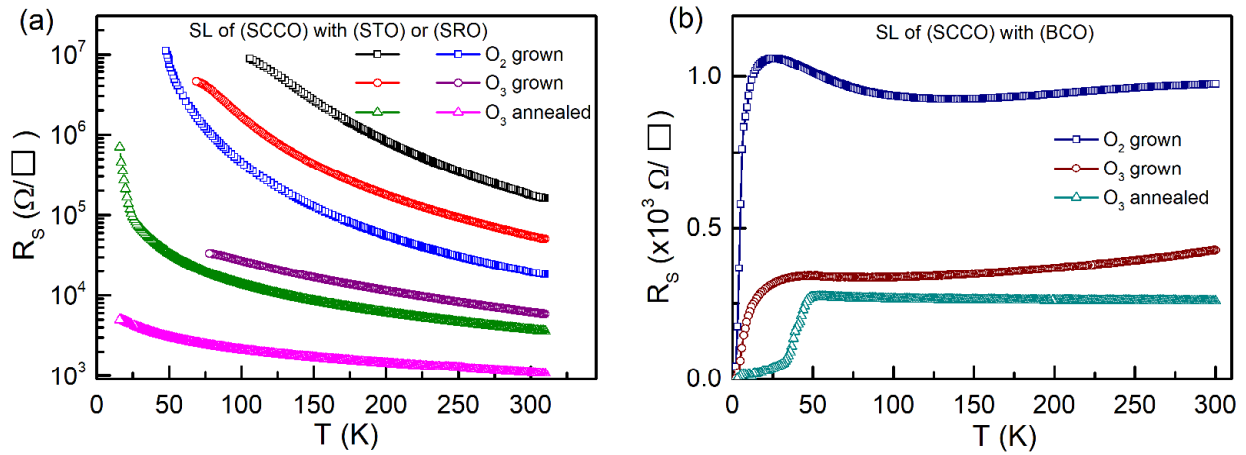
Figure 4. Temperature-dependent sheet resistance for **(a)** $[(SCCO)_8/(STO)_4]_{10}$, $[(SCCO)_8/(SRO)_4]_{10}$ and **(b)** $[(SCCO)_8/(BCO)_1]_{10}$ SLs under various conditions (O_2-grown, O_3-grown, and O_3-annealed, respectively squares, circles and triangles).
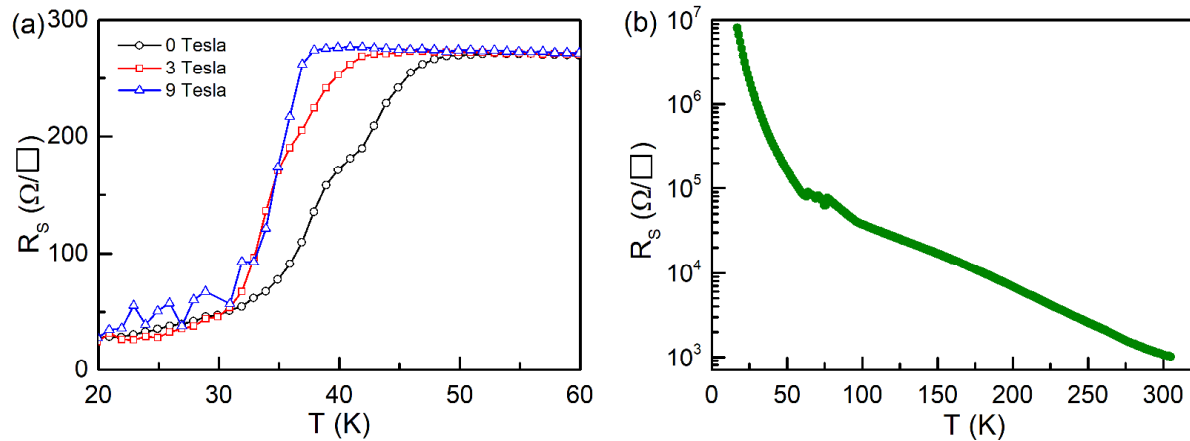

Figure 5. Temperature-dependent sheet resistance for **(a)** $[(SCCO)_8/(BCO)_1]_{10}$ SL (O_3-annealed) under the application of a magnetic field. **(b)** Zero field temperature-dependent sheet resistance for $[(SCCO)_8/(STO)_2/(BCO)_1/(STO)_2)]_{10}$ SL (O_3 -annealed).
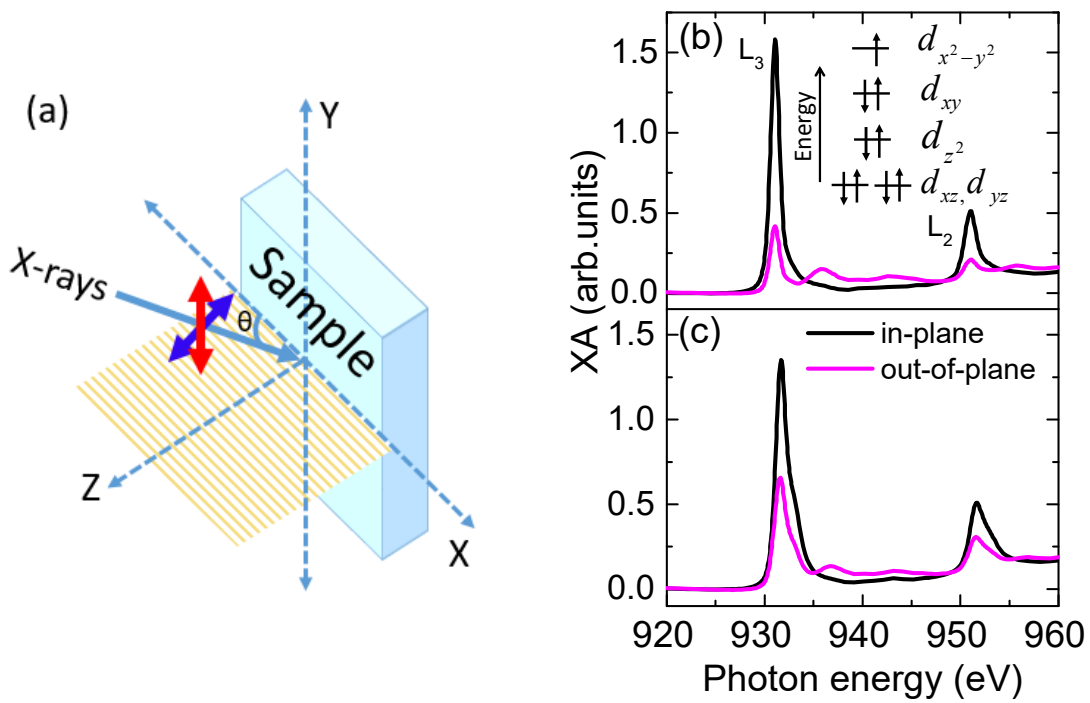
Figure 6. Schematic (a) XA measurement geometry. XA spectra for **(b)** [(SCCO)$_8$/(STO)$_4$] and **(c)** [(SCCO)$_8$/(SRO)$_4$] SLs respectively. The inset in **(b)** schematically shows the square planar crystal-field energy levels with electronic occupation at the Cu site in the SCCO layer.
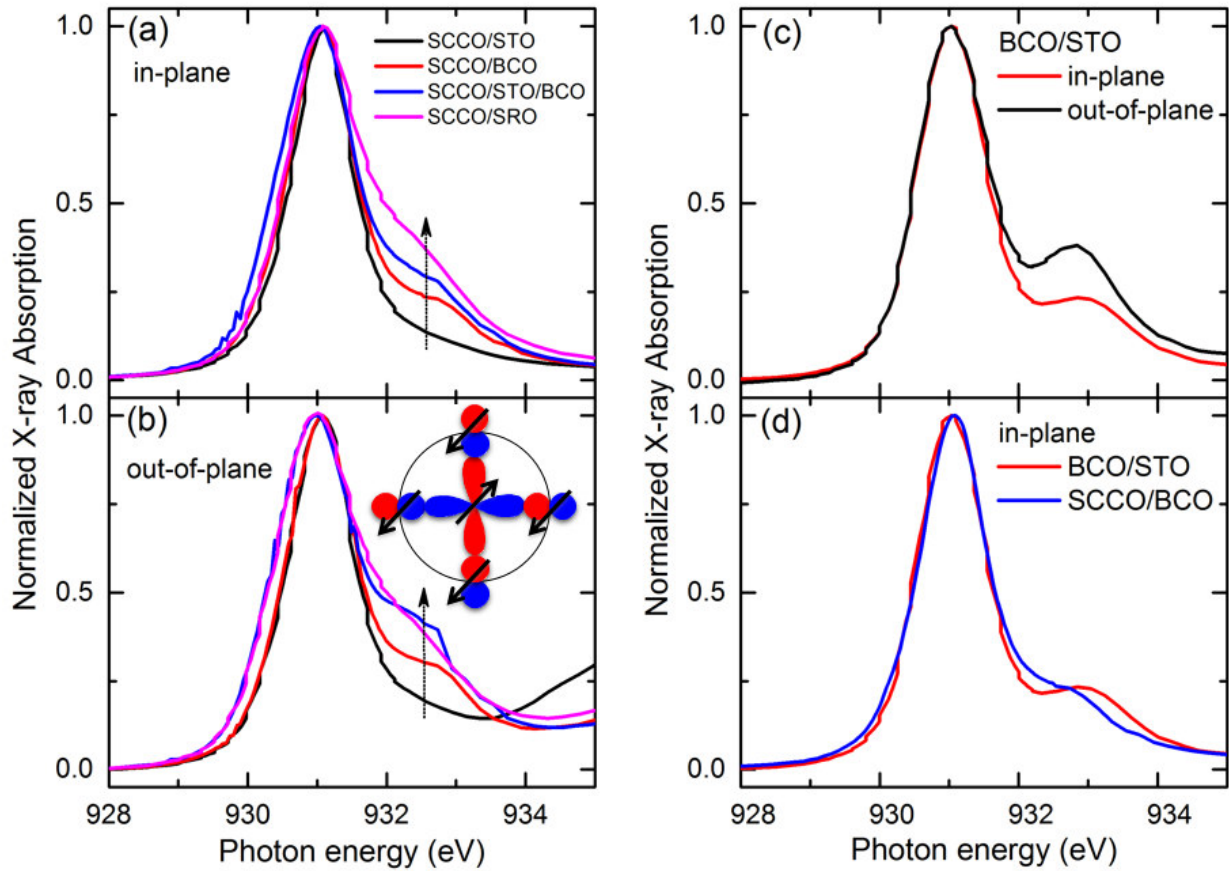
Figure 7. XA spectra normalized to the maximum height intensity of the L_3 peak for $[(SCCO)_8/(STO)_4]$, $[(SCCO)_8/(BCO)_1]$, $[(SCCO)_8/(STO)_2/(BCO)_1/(STO)_2]$ and $[(SCCO)_8/(SRO)_4]$ SLs for the polarization in the **(a)** in-plane and **(b)** out-of-plane directions. The arrow indicates the region of the ligand hole state. The inset shows the schematic of the ZRS structure. **(c)** XA spectra of the L_3 peak for the $[(BCO)_1/(STO)_3]$ SL in both polarization directions. **(d)** Difference in the spectral intensity shape of the L_3 peak belonging to ligand states between the coupled (chain and plane) [SCCO/BCO] SL and chain type only BCO layer.

Supplemental Material

Unusual structural rearrangement and superconductivity in infinite layer cuprate superlattices

D. Samal,[1,2,#,*] Nicolas Gauquelin,[3,#,*] Yayoi Takamura,[4] Ivan Lobato,[3] Elke Arenholz,[5] Sandra Van Aert,[3] Mark Huijben,[6] Zhicheng Zhong,[7] Jo Verbeeck,[3] Gustaaf Van Tendeloo,[3] Gertjan Koster[6,*]

[1]Institute of Physics, Sachivalaya Marg, Bhubaneswar 751005, India

[2]Homi Bhabha National Institute, Anushakti Nagar, Mumbai 400085, India

[3]EMAT, University of Antwerp, Groenenborgerlaan 171, 2020 Antwerp, Belgium

[4]Department of Materials Science and Engineering, University of California-Davis, Davis, California 95616, United States

[5]Advanced Light Source, Lawrence Berkeley National Laboratory, Berkeley, California 94720, United States

[6]Faculty of Science and Technology, MESA+ Institute for Nanotechnology, University of Twente, 7500 AE Enschede, The Netherlands

[7]Key Laboratory of Magnetic Materials Devices & Zhejiang Province Key Laboratory of Magnetic Materials and Application Technology, Ningbo Institute of Materials Technology and Engineering, Chinese Academy of Sciences, Ningbo 315201, China

[#]equally contributing authors

[*]Corresponding authors

g.koster@utwente.nl, Nicolas.Gauquelin@uantwerpen.be, dsamal@iopb.res.in

Keywords: Atomic layer engineering, infinite layer cuprates, superconductivity, X-ray absorption, scanning transmission electron microscopy.

1. Growth of thin film superlattices

Infinite layer (IL)-based cuprate superlattices (SLs) consisting of an 8 unit cell (uc) layer of $Sr_{0.6}Ca_{0.4}CuO_2$ (SCCO) sandwiched between ultrathin spacer layers-$SrTiO_3$ (STO), $SrRuO_3$ (SRO) or $BaCuO_2$ (BCO), were grown by pulsed laser deposition (PLD) in a layer by layer fashion on TiO_2 terminated STO substrate. Various SLs of the form $[(SCCO)_8/(STO)_4]_{10}$, $[(SCCO)_8/(SRO)_4]_{10}$, $[(SCCO)_8/(BCO)_1]_{10}$ and $[(SCCO)_8/(STO)_2/(BCO)_1/(STO)_2]_{10}$ were grown and studied. For the sake of brevity, we represent the above SLs as [SCCO/STO], [SCCO/SRO], [SCCO/BCO] and [SCCO/STO/BCO/STO] respectively. *In situ* reflection high energy electron diffraction (RHEED) was used to monitor the growth at unit cell (uc) level. To grow the complete stack of SL structure, the number of laser pulses required for each layer of a specific material was calibrated and then the growth was performed in accordance with the periodicity of SL required. In **Figure** S1, we show the RHEED intensity oscillations during film growth and in **Figure** S2,we show the representataive RHEED pattern for various SLs.
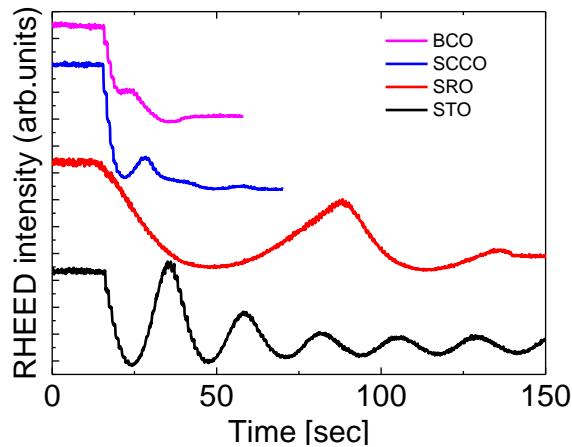

Figure S1: RHEED intensity oscillation during the thin film growth.
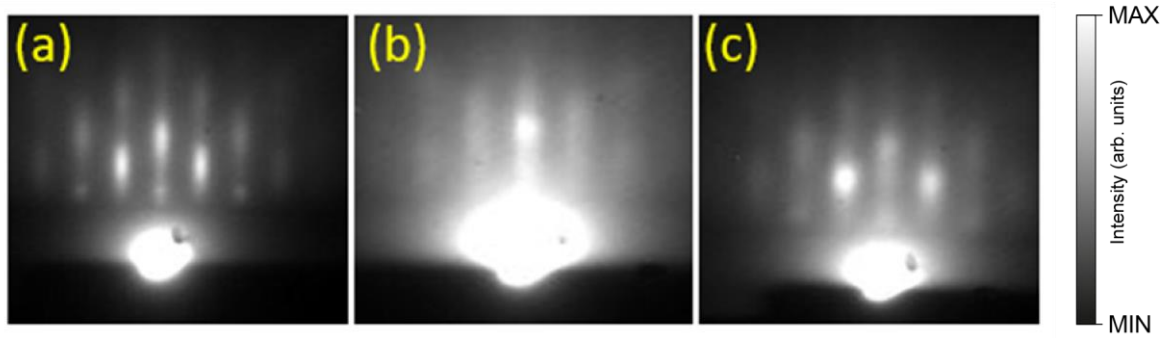
2

Figure S2: Representataive RHEED pattern for (a) [SCCO/STO] , (b) [SCCO/BCO] and (c) [SCCO/STO/BCO/STO] SLs.

2. X-ray diffraction (XRD)

In **Figure** S3, we show the typical $\theta - 2\theta$ X-ray diffraction pattern for [SCCO/STO], [SCCO/SRO] and [SCCO/BCO] SLs. A signature of satellite peaks corresponding to the SL structure is observed in all cases, which demonstrates the structural quality of the SLs. The satelite peaks in [SCCO/SRO] SL shows a splitting and in case of [SCCO/STO] SL, a broad shoulder corresponding to the film is noticed around ~ 47°.
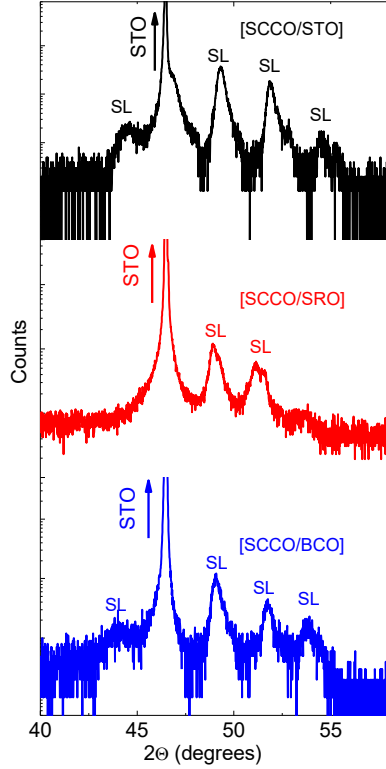
Figure S3: $\theta - 2\theta$ XRD patterns of SLs [(SCCO)$_8$/(STO)$_4$]$_{10}$, [(SCCO)$_8$/(SRO)$_4$]$_{10}$ and [(SCCO)$_8$/(BCO)$_1$]$_{10}$, where the intense peak marked by the arrow corresponds to the STO substrate and the peaks indexed by SL refers to distinct satellite peaks corresponding to the SL structure.

3. Transmission Electron microscopy (TEM)

In **Figure** S4(a), we show the raw annular dark field (ADF), annular bright field (ABF), inversed ABF (iABF), and a false color RGB image combining the ADF image in red, the ABF image in blue and the iABF image in green in order to better vizualize the difference between heavy and light atomic columns. For the [SCCO/STO] SL (**Figure** S4(a)), we can notice at the top interface of the second STO layer a full unit cell step (TiO$_2$ layer as termination layer). In case of [SCCO/SRO] SL (**Figure** S4(b)) we can notice darker contrasts in ADF and brighter contrasts in ABF in most of the SCCO layers, in some of these we can even see additional oxygen columns present between the infinite layers. This is related to formation of domains with different orientations within the SCCO layers and confers a wavy-character to some of the

SRO layers. For [SCCO/BCO] SL (**Figure** S4(c)), we can notice that when the BCO layers appear thicker than a unit cell, the atomic contrast in those layers look more diffuse. We attribute this to steps being present within the thickness of the sample as can be seen in **Figure** S5(a). The fact that those steps marked by arrows are just one atomic plane high and not one uc high makes us believe that these are related to the plane-chain instability occuring due to the atomic roughness and very close chemical composition of the SCCO and BCO layers. Therefore, we interpret the contrast in regions with more than 3 atomic planes in the BCO layer to be related to projection effects related to the presence of steps due to this roughness within the thickness of the TEM sample (around 20 nm). We thereafter consider the BCO layer to be always 1uc thick on the local scale.
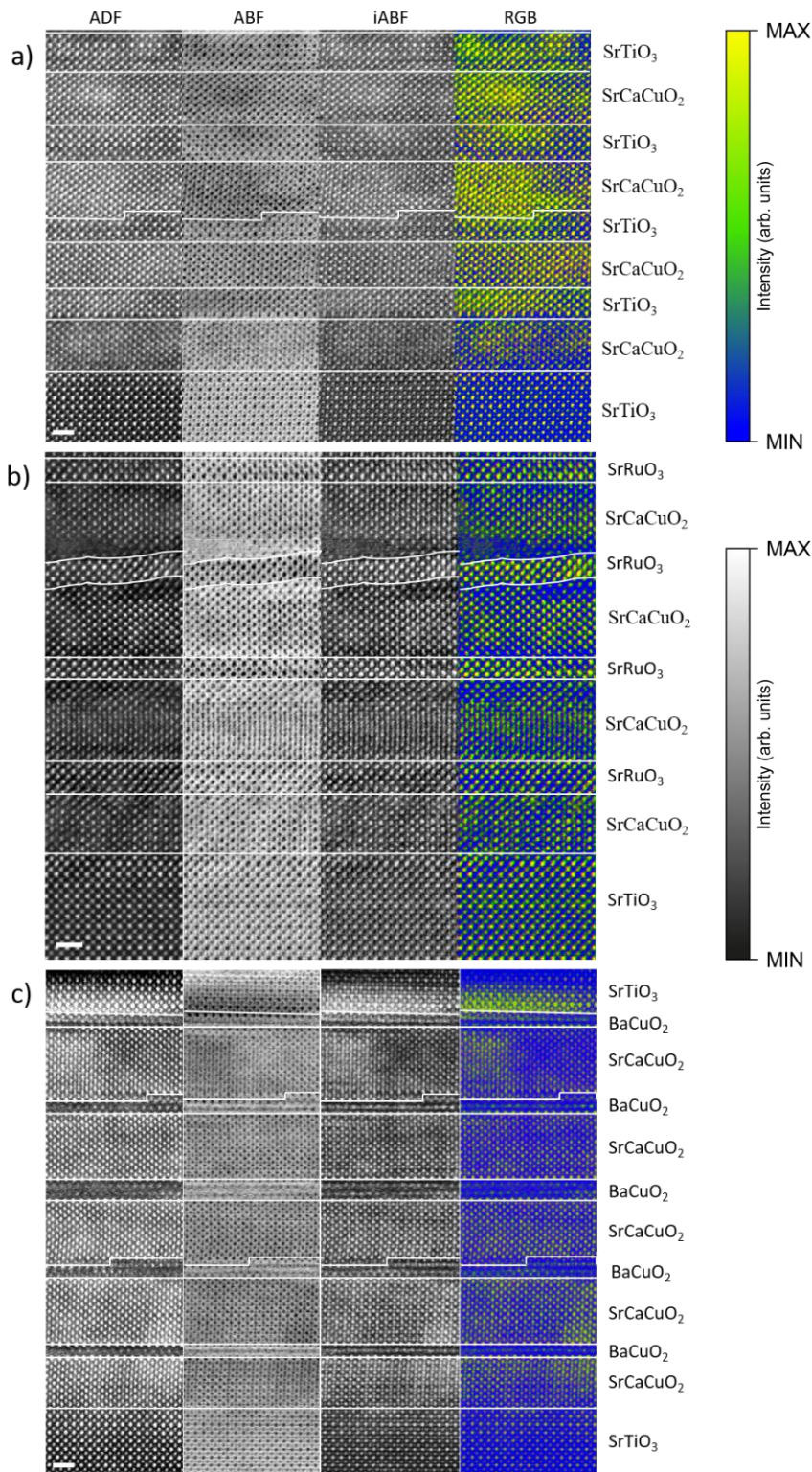
Figure S4: Raw ADF, ABF and inversed ABF (iABF) with the RGB image combining HAADF in red, iABF in green, and ABF in blue of (a)[SCCO/STO], (b) [SCCO/SRO], and (c) [SCCO/BCO] SLs. The white lines are guides to the eye to identify the location of the interfaces. Scale bar is 1nm.
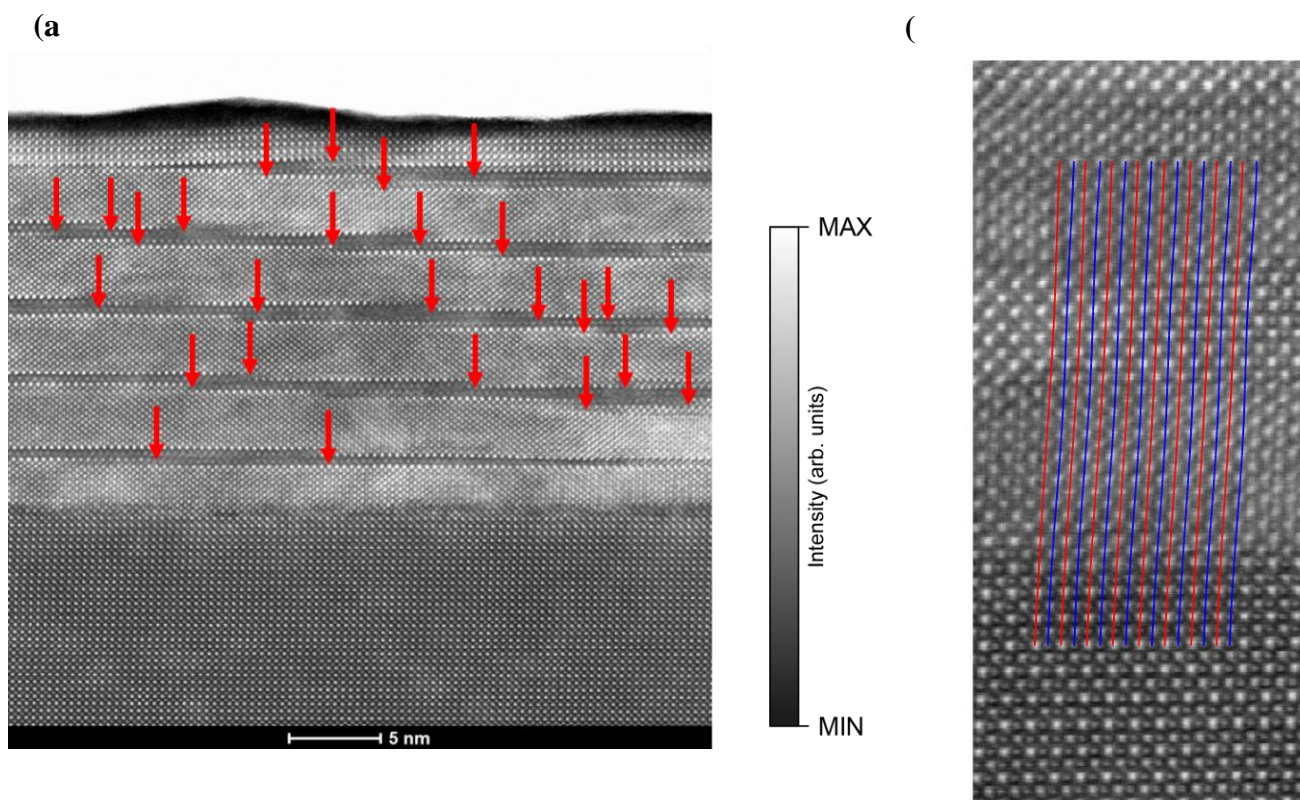
(a

(

Figure S5:(a) HAADF images of [SCCO/BCO] SL showing the presence of many steps marked with red arrows (b) part of the iABF image (presented in **Figure** S4(a), panel 3) explaining the lines used to get the profiles shown in Figures 2(a) (same methodology was applied to get profiles shown on figures 2(b-c) and Figure 3(c-d). Scale bar is 1 nm.

Figure S6 presents the STEM-EELS (electron energy loss spectroscopy) analysis of the [SCCO/STO/BCO/STO)] SL. An energy dispersion of 1eV/pixel was used to collect the Cu $L_{2,3}$ Ba $M_{4,5}$ the Ti $L_{2,3}$ and Ca $L_{2,3}$ edges in the EELS spectrum. The edge maps are presented in **Figure** S6. These spatially resolved maps are then combined in a color map showing rather good epitaxy of the different layers with Ca in yellow, Cu in red, Ti in blue and Ba in green. The region displayed has the following sequence from bottom to top: BaO-$(SrTiO_3)_2$-$(SCCO)_7$-$(SrTiO_3)_2$-$(BaCuO_x)_2$-$(SrTiO_3)_2$-$(SCCO)_6$-$(SrTiO_3)_2$-BaO.
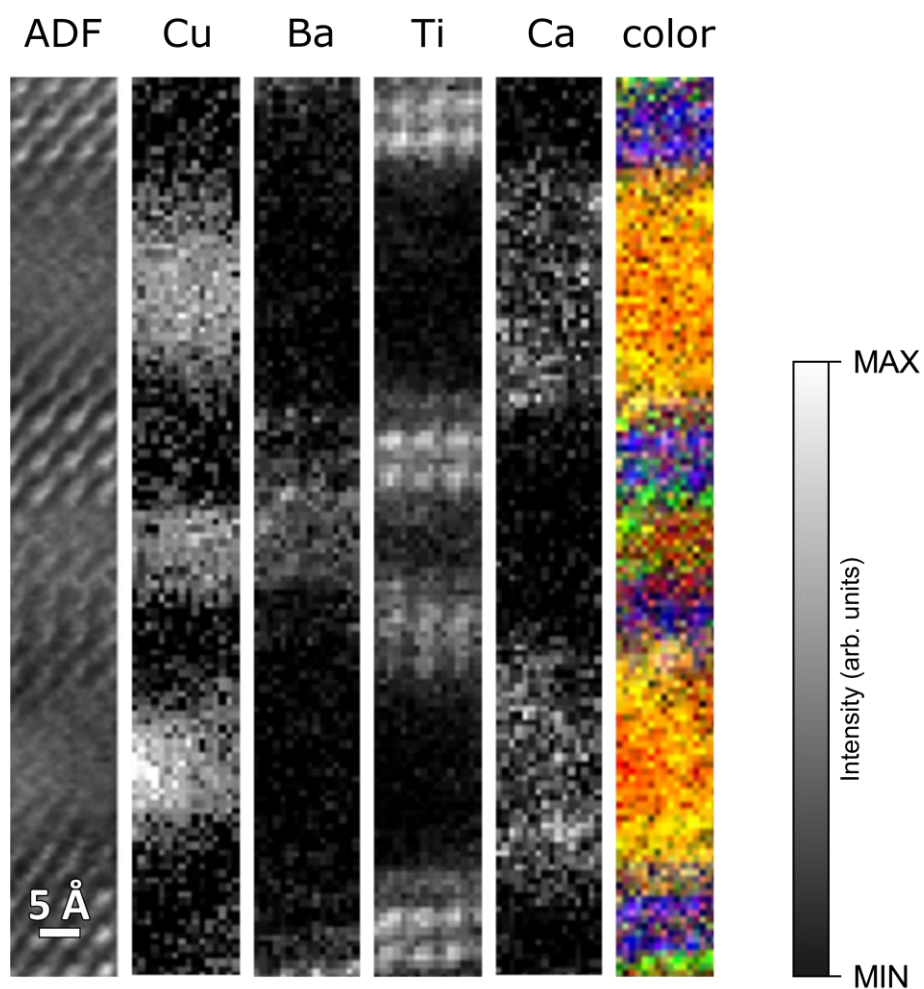
Figure S6: STEM-EELS analysis of the [SCCO/STO/BCO/STO] SL showing from left to right the ADF signal, the Cu $L_{2,3}$ edge, the Ba $M_{4,5}$ edge, the Ti $L_{2,3}$ edge and the Ca $L_{2,3}$ edge. These edge maps are combined in a color map showing the rather good epitaxy of the different layers (Ca in yellow, Cu in red, Ti in blue and Ba in green).

4. Electrical transport on [SCCO/BCO] SL

For ease of comparison of superconducting transition in [SCCO/BCO] SL under various growth conditions (O_2-grown, O_3-grown, and O_3-annealed, respectively), we have shown the temperature dependent R_S (T)/R_S (80 K) and normalized (dR_s/dT) plots in Figure S7. It is apparent that the onset of the superconducting transition for O_3-annealed [SCCO/BCO] SL, is enhanced up to ~50 K and moreover the transition region gets widened.
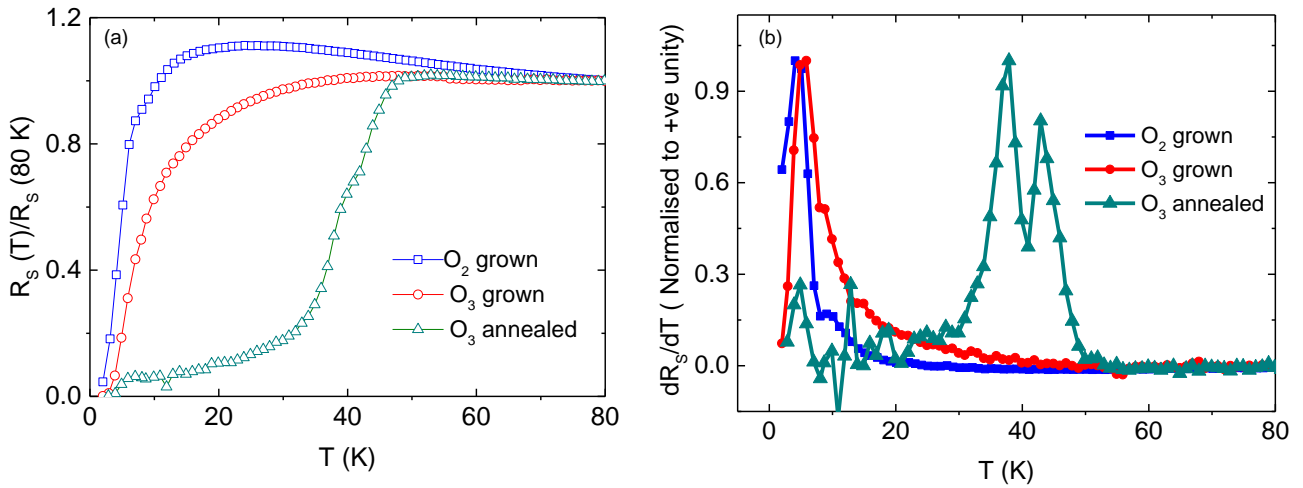

Figure S7: (a) Temperature dependent R_S (T)/R_S (80 K) and (b) normalized (dR_s/dT) plots for $[(SCCO)_8/(BCO)_1]_{10}$ SL under various conditions (O_2-grown, O_3-grown, and O_3-annealed, respectively)